Material metrics for laser cooling of solids

Jedo Kim, Ankur Kapoor, and Massoud Kaviany*
Department of Mechanical Engineering, University of Michigan, Ann Arbor, Michigan 48109-2125, USA
(Received 4 December 2007; revised manuscript received 8 February 2008; published 19 March 2008)

The material metrics for optimal laser cooling of ion-doped solids are derived using atomic and molecular dynamics properties of the constituents. The anti-Stokes process is modeled as an optical phonon coupling of the bound electron, followed by a photon absorption. The transition dipole moment is estimated using a simplified charge-displacement model and the Judd–Ofelt theory of rare-earth ions both suggesting that transitions with high-energy gaps and similar angular momentum states should be used. The electron-phonon coupling is interpreted as a derivative of electronic energy with respect to displacement of the nearest neighboring ligands whose stretching mode frequency is approximated using the molecular data. The Debye-Gaussian model is used for the phonon density of states of diatomic crystal. Then, the Fermi golden rule is used for photon-induced, phonon-assisted electronic transition probability and applied to the cooling rate equation by defining a phonon-assisted transition dipole moment. Based on the material metrics, an example blend is investigated for its cooling performance and a general guide is proposed for selection of better performing laser cooling hosts. Furthermore, the cooling rate limits are discussed and three distinct characteristic times are identified with the photon-induced, phonon-assisted transition time controlling the rate. The metrics guide the selection of host materials for optimal cooling, and predict a noticeable increase in the absorption rate when using a blend of cation atoms.

DOI: 10.1103/PhysRevB.77.115127 PACS number(s): 78.20.Nv, 78.20.Bh, 78.55.Hx

I. INTRODUCTION

Laser cooling of solids is achieved when a photon having a lower frequency (energy) excites an electron with assistance from a phonon and this is followed by a single photon emission with a mean frequency higher than that of the incident photon (i.e., anti-Stokes process). Pringsheim[1] recognized the possibility of the anti-Stokes process which was later confirmed experimentally by Epstein *et al.*[2] in the first successful experiment of laser cooling of solids. The entropy aspect of laser cooling of solids is discussed in Ref. 3 and a general review is given in Ref. 4. Host materials including ZBLAN (ZrF_4-BaF_2-LaF_3-AlF_3-NaF),[5] ZBLANP (ZBLAN-PbF_2),[6] YAG ($Y_3Al_5O_{12}$), CNBZn (CdF_2-$CdCl_2$-NaF-BaF_2-$BaCl_2$-ZnF_2), and KPb_2Cl_5 (Ref. 7) have been doped with various rare-earth ions, e.g., Yb^{3+}, Er^{3+}, and Tm^{3+}, and successfully laser cooled. In contrast to experimental successes, the theoretical extension of the anti-Stokes process has not advanced far, from the formulation by Pringsheim.[1] Thus, the theoretical approach to laser cooling of solids has not allowed for predictive selection of materials for efficient cooling. Recent theoretical analyses address localized electrons[8] and strong electron-phonon coupling.[9] However, further investigation of the interaction amongst the three carriers, namely, photon, electron, and phonon, is needed. Here we propose material selection metrics using simplified theoretical models for the three-carrier interactions, and suggest possible improvements in the materials selection.

Figures 1(a)–1(c) demonstrate the materials, i.e., atomic and molecular dynamics (MD), metrics of the photon-electron-phonon interactions in laser cooling of Yb^{3+}-doped solids. The photon-induced, phonon-assisted absorption process is modeled as a phonon absorption, followed by a photon absorption. Three steps are identified: (a) phonon-assisted absorption, (b) radiative decay, and (c) nonradiative (purely phonon) decay. These are designated by their kinetics represented by phonon-assisted transition time $\tau_{ph\text{-}e\text{-}p}$, purely radiative decay $\tau_{e\text{-}ph}$, and purely phonon decay $\tau_{e\text{-}p}$ where subscripts *ph*, *e*, and *p* represent photon, electron, and phonon, respectively.

As shown in Fig. 1(a), the electron (in ion) oscillates between the ground level manifolds due to continuous excitation by phonons (thermal vibrations). At the same time, due to changes in the position of the immediate neighboring atom, the electronic wave function is altered resulting in oscillations of the energy levels within the manifold. This reflects the observed thermal broadening. Since the energy levels of the manifolds are quantized and discrete, only allowed phonons corresponding to the energy level difference are able to promote electrons between these levels. Conversely, when the energy spacings of the oscillating ground-state manifold matches the available phonon modes, the electron is promoted to a higher-energy level within the manifold. Note that the these energy levels should exist within the limits defined by the Heisenberg uncertainty theorem, which is related to the natural broadening of these energy levels.[10] In the vicinity of the doped ions, the available local modes are characterized by the normal modes of the ion-ligand complex, which have attributes of optical phonon due to the breathing mode. The displacement due to longitudinal optical phonon is represented by Δ_p. For the rare-earth ions, the optically active f^n shell electron is well localized (within the atomic spacing of the ion-ligand complex), thus the short-wavelength phonons become important. The electron interaction with optical phonons will be discussed in the subsequent sections. When a photon is introduced, the photon encounters an electron in oscillation and promotes it to the excited level. This process is not only a function of the availability of phonons, but also a function of the transition dipole moment (electron transition overlap integral). Therefore, we

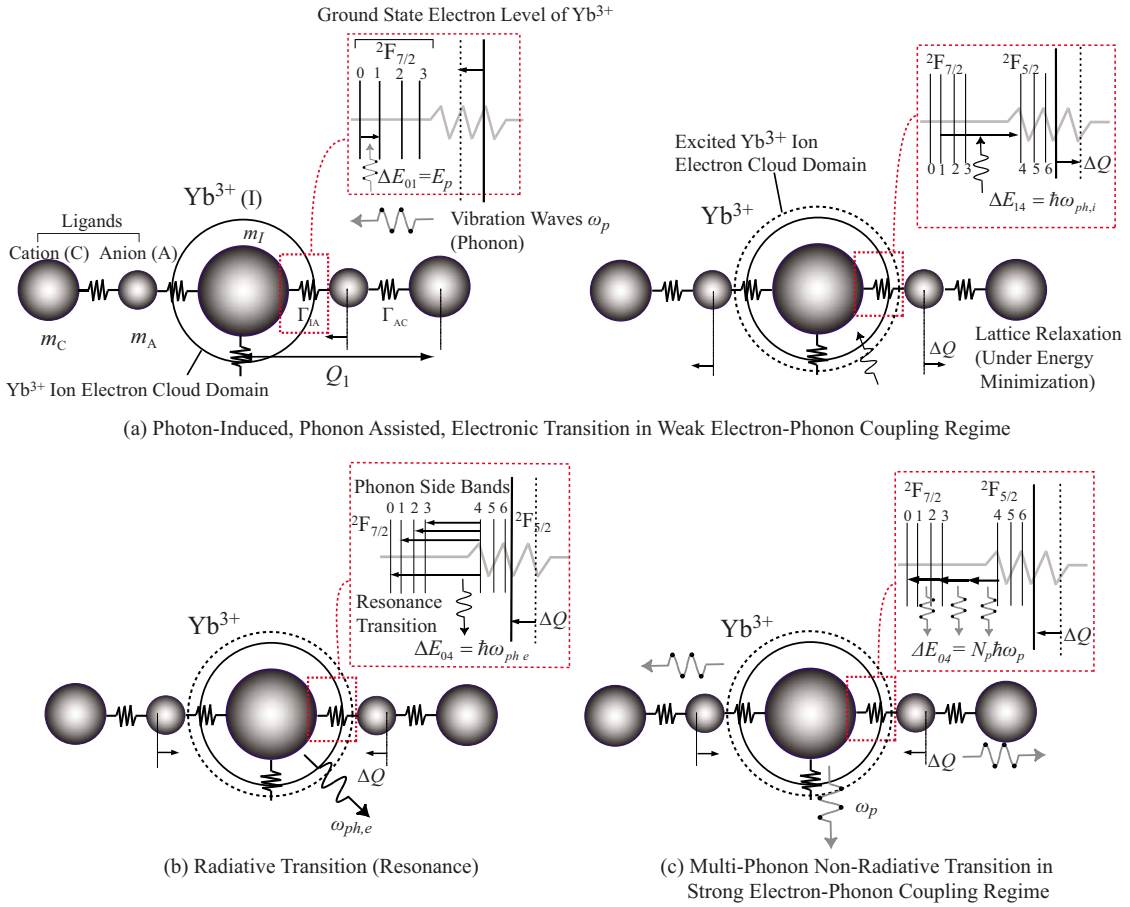

FIG. 1. (Color online) Material (atomic and MD) metrics of the photon-electron-phonon interactions in laser cooling of Yb^{+3}-doped solids. (a) Model for the optical phonon coupling with a bound electron followed by photon absorption. (b) Purely radiative emission process. The phonon side band transitions are also shown. (c) Purely nonradiative emission process.

examine the transition dipole moment as well as phonon availability. When the electron is promoted to the excited state, it has multiple paths through which it can decay back to the ground state: purely radiative, purely nonradiative, and vibronic transitions. Purely radiative decay process is shown in Fig. 1(b). The electron directly decays to the lowest lying ground level by emitting a photon having a frequency equal to its resonance transition frequency. This decay process is normally the strongest transition at moderate temperatures. Figure 1(c) shows the purely nonradiative process in which the electron is deexcited by emitting multiple phonons simultaneously. This process dominates at high temperatures. Nevertheless, for the rare-earth ions in a crystal, the purely nonradiative decay is suppressed, because of the weak electron-phonon interaction strength due to the localization of optically active f^n electron shell. This is one of the motivations of using rare-earth doped solids. Lastly, the electron also can be deexcited by a vibronic process, i.e., emitting a photon and a phonon that is, the opposite process of photon-induced, phonon-assisted electron absorption.

The emission spectrum (dimensionless $E^*_{ph,e}$) of Yb^{3+}: ZBLANP is shown in Fig. 2(a).[11] Apart from the strongest resonance transition $(^2F_{5/2})_4 \rightarrow (^2F_{7/2})_0$, there exist three phonon side-band transitions designated as (1,2,3). When the mean absorbed phonon energy is larger than the average emitted phonon (the three vibronic transitions), cooling occurs. The conditions for cooling and/or heating are

$$\hbar\omega_{ph,i} - \hbar\bar{\omega}_{ph,e} = \hbar\omega_p < 0 \quad \text{cooling (anti-Stokes process)}, \tag{1}$$

$$\hbar\omega_{ph,i} - \hbar\bar{\omega}_{ph,e} = \hbar\omega_p > 0 \quad \text{heating (Stokes process)}, \tag{2}$$

where $\omega_{ph,i}$ is the incoming photon frequency, $\bar{\omega}_{ph,e}$ is the average emission photon frequency, and ω_p is the phonon frequency. The absorption spectrum (dimensionless $E^*_{ph,a}$) of Yb^{3+}: ZBLANP in Fig. 2(b) shows that there are also three sublevels in the excited state manifold. The spectrum indicates that the absorption intensity of the phonon-assisted transition can be an order of magnitude lower than the resonance transition. This reflects small second-order transition rate which involves all three carriers compared to that of the first-order process rate. One reason for such low transition rate is the mismatch between normal modes of the ion-ligand complex and the maximum available normal mode energy of the crystal, resulting in a low cooling rate. Figure 3 shows a typical variation of the normalized cooling rate for a diatomic crystal with respect to phonon energy. The discrete

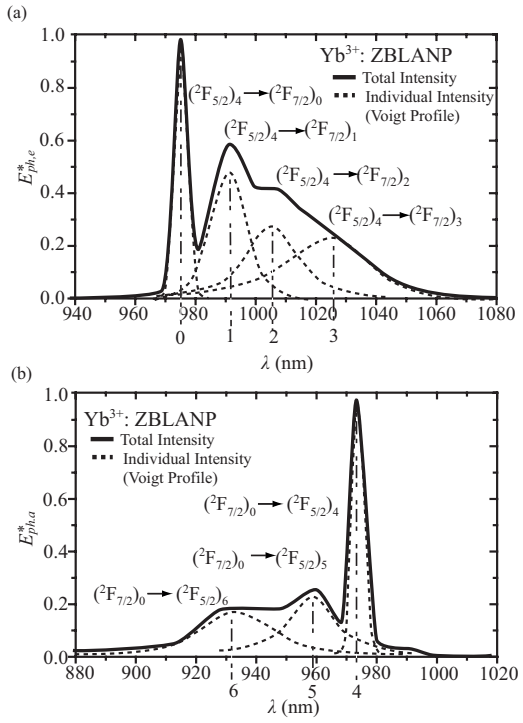

FIG. 2. (a) Dimensionless emission spectrum of Yb^{3+}: ZBLANP at $T=10$ K. The transitions $(^2F_{5/2})_4 \rightarrow (^2F_{7/2})_{0,1,2,3}$, from the first excited manifold to four ground level manifolds are extrapolated (Voigt profile) and are also shown. (b) Dimensionless absorption spectrum of Yb^{3+}: ZBLANP at $T=10$ K (Ref. 11).

energy level of the ground electronic state oscillates due to presence of phonons. The absorption rate is proportional to the product of this discrete energy level and the available phonon modes within the lattice. Since this absorption rate is directly proportional to the cooling rate, cooling peak is observed. Now we discuss the three-carrier interaction process in detail.

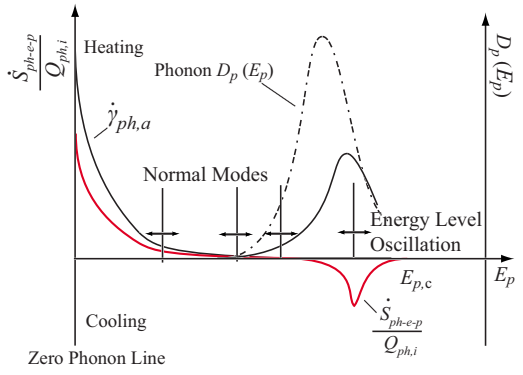

FIG. 3. (Color online) Typical normalized cooling rate, as a function of phonon energy, for a diatomic crystal using the Debye-Gaussian model of phonon density of state D_p. The discrete normal modes of the complex do not correspond to the available phonon modes of the crystal resulting in a low cooling rate. $\dot{\gamma}_a$, absorption rate, and the energy level oscillation are also shown.

A. Radiative transition rate

The fastest transition process in laser cooling is the purely radiative transition which is a first-order transition process between photon and electron. Purely radiative transition is represented by an electric-dipole transition approximation between the two states having a nonzero matrix element in the dipole moment integral.

The total Hamiltonian of the system is

$$H = H_e + H_{ph} + H_{ph\text{-}e}. \tag{3}$$

The first term is

$$H_e = \hbar \omega_{e,g} a^\dagger a, \tag{4}$$

which is the Hamiltonian of the ion electronic levels, where $\hbar\omega_{e,g}$ is the energy difference between the optically active energy levels of the dopant ion, and $a^\dagger(a)$ is the creation (annihilation) operator of an electronic excitation. The second term is

$$H_{ph} = \hbar \omega_{ph,i} c^\dagger c, \tag{5}$$

which is the electromagnetic laser field Hamiltonian, where $\omega_{ph,i}$ is the incoming photon frequency and $c^\dagger(c)$ is the creation (annihilation) operator of a photon. The third term is

$$H_{ph\text{-}e} = -\boldsymbol{s}_{ph,i} \cdot \boldsymbol{\mu}_{ph\text{-}e} \left(\frac{\hbar \omega_{ph,i}}{2\epsilon_o V} \right)^{1/2} (c^\dagger + c)(a^\dagger + a), \tag{6}$$

which is the photon-electron interaction Hamiltonian where $\boldsymbol{s}_{ph,i}$ is the polarization vector of photon, $\boldsymbol{\mu}_{ph\text{-}e}$ is the dipole moment vector of electronic transition, ϵ_o is the vacuum permittivity, and V is the interaction volume.

Now, the Fermi golden rule is used to calculate the total transition rate $\dot{\gamma}_{ph\text{-}e}$ as[12]

$$\dot{\gamma}_{ph\text{-}e} = \sum_f \dot{\gamma}_{e,i\text{-}f} = \frac{2\pi}{\hbar} \sum_f |M_{f,i}|^2 D_{ph} = \frac{2\pi}{\hbar} |M_{f,i}|^2 \frac{\kappa^2 d\Omega}{\hbar u_{ph} (2\pi)^3} V, \tag{7}$$

where $M_{f,i}$ is the interaction matrix element and D_{ph} is the photon density of states given by $\kappa^2 d\Omega d\kappa V/(2\pi)^3 dE_{ph}$ with $dE_{ph}=\hbar u_{ph} d\kappa$, Ω is the solid angle, κ is the wave number, and u_{ph} is speed of light. Since the two states of the electron have nonzero matrix element, the transition allowed is first order and the interaction matrix element $M_{f,i}$ is expanded as

$$M_{f,i,1st} = \langle f | H_{int} | i \rangle = \langle \varphi_f, f_{ph} | H_{ph\text{-}e} | \varphi_i, f_{ph} + 1 \rangle, \tag{8}$$

where f_{ph} is the photon distribution function. Then using Eqs. (6) and (7) the transition rate becomes

$$\dot{\gamma}_{ph\text{-}e} = \frac{1}{\tau_{ph\text{-}e}} = \frac{\omega_{e,g}^3}{3\pi\epsilon_o \hbar u_{ph}^3} \mu_{ph\text{-}e}^2, \tag{9}$$

which is the definition of the Einstein A coefficient (we have used $\omega=\kappa u_{ph}$). For spontaneous emission process, the initial and final states in Eq. (8) are switched, i.e., $\langle \varphi_f, f_{ph}+1 | H_{ph\text{-}e} | \varphi_i, f_{ph} \rangle$, but the transition rate $\tau_{e\text{-}ph}$ is given by Eq. (9).

B. Local, vibrational-mode assisted transition rate

The photon-induced, phonon-assisted transition is the essence of the anti-Stokes process. Thus, determining the physical parameters which affect the entire process is important. To account for the transition rate for the photon-induced, local vibrational mode assisted electronic transition rate of the optically active ion, we modify the electron-phonon interaction Hamiltonian in the cooling rate equation, as described in Refs. 13 and 14 to include the electron-optical phonon interaction.

Similar to the radiative transition, the Hamiltonian of the entire system is

$$H = H_e + H_p + H_{ph} + H_{ph\text{-}e} + H_{e\text{-}p}. \tag{10}$$

The first term is the electron Hamiltonian defined before, the second term is

$$H_p = \sum_p \hbar \omega_p b^\dagger b, \tag{11}$$

which is the phonon field Hamiltonian, where ω_p is the phonon frequency and $b^\dagger(b)$ is the creation (annihilation) operator of a phonon in mode p. The third and fourth terms are photon field and electron-photon interaction Hamiltonian, respectively, defined before.

The fifth term is the electron-phonon interaction Hamiltonian described as distortion of the ligand ions affecting the crystal field. Such a distortion is a function of local strain; therefore, we expand the crystal field potential in powers of such strain. The local strain is defined by the strain term $\epsilon_{i,j}$ as

$$\epsilon_{i,j} = \frac{1}{2}\left(\frac{\partial d_i}{\partial x_j} + \frac{\partial d_j}{\partial x_i}\right) \quad (i,j = 1,2,3). \tag{12}$$

For simplicity we use

$$\epsilon \approx \left.\frac{\partial d}{\partial x}\right|_{x=0}, \tag{13}$$

i.e., not taking into any account the anisotropy of the elastic waves. The origin of the coordinate is the point in the lattice where the ion nucleus is located. The derivative of the displacement d is set to be the normal coordinate,

$$Q_q = \left.\frac{\partial d}{\partial x}\right|_{x=0} = \left(\frac{\hbar}{2m_{\mathrm{AC}}\omega_p}\right)^{1/2}(b + b^\dagger), \tag{14}$$

where q specifies a particular mode. When a particular mode of vibration dominates the electron-phonon interaction, we express the electron-phonon interaction Hamiltonian in terms of the normal coordinates. Using the optical deformation potential theory, the crystal field Hamiltonian term becomes[15]

$$H_c = H_{\mathrm{o}} + \varphi'_{e\text{-}p,\mathrm{O}} Q_q. \tag{15}$$

The higher-order terms have been neglected. Then the interaction Hamiltonian term becomes

$$H_{e\text{-}p} = \varphi'_{e\text{-}p,\mathrm{O}} Q_q = \varphi'_{e\text{-}p,\mathrm{O}}\left(\frac{\hbar}{2m_{\mathrm{AC}}\omega_p}\right)^{1/2}(b_q + b_q^\dagger), \tag{16}$$

where $\varphi'_{e\text{-}p,\mathrm{O}}$ is the electron-phonon coupling potential, ω_p is the phonon frequency, and m_{AC} is the effective mass of the oscillating atoms.

Then the second-order term of the perturbation expansion gives the transition (absorption) rate $\dot{\gamma}_{ph\text{-}e\text{-}p}$ (the Fermi golden rule) as

$$\dot{\gamma}_{ph\text{-}e\text{-}p} = \sum_f \dot{\gamma}_{e,i\text{-}f} = \frac{2\pi}{\hbar}\sum_f |M_{f,i}|^2 \delta_{\mathrm{D}}(E_{e,f} - E_{e,i}), \tag{17}$$

where $E_{e,i}$ and $E_{e,f}$ are, respectively, the initial and final energies of the electron system, and δ_{D} is the Dirac delta. The $M_{f,i}$ matrix admits a second-order perturbative expansion as

$$M_{fi,2\mathrm{nd}} = \sum_m \frac{\langle f|H_{int}|m\rangle\langle m|H_{int}|i\rangle}{E^T_{e,i} - E^T_{e,m}} \simeq \sum_m \frac{\langle \psi_f, f_{ph}, f_p|H_{ph\text{-}e}|\psi_m, f_{ph}+1, f_p\rangle\langle \psi_m, f_{ph}+1, f_p|H_{e\text{-}p}|\psi_i, f_{ph}+1, f_p+1\rangle}{E_i - (E_m - \hbar\omega_p)}. \tag{18}$$

When the interaction matrix is rewritten using the Hamiltonian expansion, the transition rate becomes

$$\dot{\gamma}_{ph\text{-}e\text{-}p} = \frac{\pi\hbar}{2m_{\mathrm{AC}}} \frac{(\boldsymbol{s}_{ph,i}\cdot\boldsymbol{\mu}_{ph\text{-}e})^2}{\epsilon_{\mathrm{o}}} \varphi'^2_{e\text{-}p,\mathrm{O}} \frac{D_p(E_p) f^{\mathrm{o}}_p(E_p)}{E_p^3} \frac{\hbar\omega_{ph,i} D_{ph}}{V}, \tag{19}$$

where $D_p(E_p)$ is the phonon density of states of phonon having energy E_p, f_p is the Bose–Einstein distribution function, $\omega_{ph,i}$ is the incoming photon frequency, and D_{ph} is the photon density of states which integrates to unity, since the incoming laser light is assumed to be monochromatic and one-photon interaction is assumed. Note that $D_p(E_p)$ is the phonon density of states for the normal (local) modes which may be different from that for the bulk host material.

Now, we write the cooling rate as

$$\dot{S}_{ph\text{-}e\text{-}p} = \dot{S}_{ph,a} - \dot{S}_{ph,e}, \tag{20}$$

where $\dot{S}_{ph\text{-}e\text{-}p}$ is the cooling rate, and $\dot{S}_{ph,a}$ and $\dot{S}_{ph,e}$ are the absorption and emission rates, respectively. Then it is possible to express the cooling rate in terms of the absorption power as

$$\dot{S}_{ph\text{-}e\text{-}p} = \hbar\omega_{ph,i}\dot{\gamma}_{ph\text{-}e\text{-}p}\int_V n_d \mathrm{d}V_s - \hbar\omega_{ph,e}\dot{\gamma}_{ph\text{-}e}\int_V n_d \mathrm{d}V$$

$$= \left(1 - \frac{\omega_{ph,e}}{\omega_{ph,i}}\frac{\dot{\gamma}_{e\text{-}ph}}{\dot{\gamma}_{ph\text{-}e\text{-}p}}\right)\hbar\omega_{ph,i}\dot{\gamma}_{ph\text{-}e\text{-}p}\int_V n_d dV_s. \quad (21)$$

At steady state, we assume that the absorption rate is equal to the sum of the radiative and nonradiative decay rates, i.e., $\dot{\gamma}_{ph\text{-}e\text{-}p} = \dot{\gamma}_{e\text{-}ph} + \dot{\gamma}_{e\text{-}p}$, and then the quantum efficiency is defined as

$$\eta_{e\text{-}ph} = \frac{\dot{\gamma}_{e\text{-}ph}}{\dot{\gamma}_{ph\text{-}e\text{-}p}} = \frac{\dot{\gamma}_{e\text{-}ph}}{\dot{\gamma}_{e\text{-}ph} + \dot{\gamma}_{e\text{-}p}}. \quad (22)$$

Note that this is an idealized quantum efficiency for the purpose of this theoretical analysis which does not consider the effects of defects, reabsorption, surface contamination, energy transfer, etc. Empirical study of contaminates on quantum efficiency can be found in Ref. 16. Then Eq. (21) becomes

$$\dot{S}_{ph\text{-}e\text{-}p} = \left(1 - \frac{\omega_{ph,e}}{\omega_{ph,i}}\eta_{e\text{-}ph}\right)A_{ph,a}n_d u_{ph}\int_V e_{ph,i}\mathrm{d}V$$

$$= \left(1 - \frac{\omega_{ph,e}}{\omega_{ph,i}}\eta_{e\text{-}ph}\right)\sigma_{ph,i}u_{ph}\hbar\omega_{ph,i}n_{ph,i}V, \quad (23)$$

where $A_{ph,a}$ is the absorption cross-sectional area which is defined as $A_{ph,a} = \hbar\omega_{ph,i}\dot{\gamma}_{ph\text{-}e\text{-}p}/u_{ph}\hbar\omega_{ph,i}n_{ph,i}$, n_d is the dopant concentration, $\sigma_{ph,i}$ is the absorption coefficient (which is the product of $A_{ph,a}$ and n_d), and $n_{ph,i}$ is the number of photons per unit volume. The spectral absorptance $\alpha_{ph,i}$ is related to the absorption coefficient (for optically thin solid) as

$$\alpha_{ph,i} = 1 - \exp(-\sigma_{ph,i}L) \simeq \sigma_{ph,i}L, \quad \sigma_{ph,i}L \ll 1, \quad (24)$$

and $\dot{S}_{ph,a} = \alpha_{ph,i}Q_{ph,i}$, where $Q_{ph,i}$ is the incident laser power. Then Eq. (23) becomes

$$\dot{S}_{ph\text{-}e\text{-}p} = \alpha_{ph,\lambda,i}Q_{ph,i}\left(1 - \frac{\omega_{ph,e}}{\bar{\omega}_{ph,i}}\eta_{e\text{-}ph}\right). \quad (25)$$

Using the the definition of absorptance given in Eq. (23) we have

$$\dot{S}_{ph\text{-}e\text{-}p} = \frac{\pi\hbar}{2\epsilon_o m_{AC}}\langle\mu_{ph\text{-}e}\rangle^2\varphi'^2_{e\text{-}p,O}\frac{D_p(E_p)f_p^o(E_p)}{E_p^3}\frac{\hbar\omega_{ph,i}n_d L}{u_{ph}}$$

$$\times\left(1 - \frac{\omega_{ph,e}}{\bar{\omega}_{ph,i}}\eta_{e\text{-}ph}\right)Q_{ph,i}, \quad (26)$$

for the optical phonon absorption. We have used the spatial average of the transition dipole moment, which couples with the incoming polarization, as $\langle(\mathbf{s}_{ph,i}\cdot\boldsymbol{\mu}_{ph\text{-}e})^2\rangle = (\mu_{ph\text{-}e}/3^{1/2})^2 = \langle\mu_{ph\text{-}e}\rangle^2$.

From Eq. (26), the cooling rate is a function of atomic and MD quantities, including $\varphi'_{e\text{-}p,O}$, E_p, and $D_p(E_p)$. Next, we examine these quantities in search for the optimal cooling rate.

II. ELECTRON-PHOTON INTERACTION

The electron-photon interaction is characterized by an electric dipole transition from the initial state to the final state. In order to develop material selection guidelines for choosing the rare-earth ion, we perform an order of magnitude estimation by first introducing a simplified transition dipole moment estimation based on the Hatree–Fock integrals. Then we use the Judd–Ofelt theory (semiempirical) for comparison and also use this, more accurate calculation of the transition dipole moment in the cooling rates.

A. Charge-displacement approximation for $\mu_{ph\text{-}e}$

For the rare-earth compounds, the multiplicity of the f states and related properties such as the magnetic moment and spectra indicate that for most of the rare-earth group it is a good approximation to consider f electrons as atom-like orbitals.[17] The calculation of a single particle $4f$-electron wave function in atom shows that even if these states are occupied beyond the $5s$, $5p$, and $6s$ orbitals, the charge distribution of the $4f$ electron is such that most of it is inside the sphere of maximum charge density of the $5s$ and $5p$ levels. This is attributed to the dominant role played by the effective f potential $\varphi_{4f}(r)$, a radial potential well confining the $4f$ wave function to a small region of space. The resultant wave function ψ^o_{4f} is atom-like. When the rare earth ion is in a solid, the boundary conditions and potential well change, mainly in the outer most parts of the cell, through the superposition of the atomic potential wells. The change in the potential results in a change in the electron wave function to ψ_{4f}, which can be written as the sum of the atom-like wave function and a polarization wave function ψ'_{4f}. ψ'_{4f} is taken orthogonal to ψ^o_{4f}, has a nonatomic character, and has contribution outside the sphere where $5s$, $5p$, and $5d$ electrons have their maximum charge density.[17] So, we write

$$\psi_{4f} = a_n\psi^o_{4f} + (1 - a_n^2)^{1/2}\psi'_{4f}, \quad (27)$$

where ψ_{4f}, ψ^o_{4f}, and ψ'_{4f} are normalized and a_n depends on the total amount of f character for a given configuration $4f^n$. The lower the average energy of the f-electron band in the f^n

TABLE I. Energy eigenvalues and average radii of $4f$ electrons in rare-earth ions (Ref. 18).

z	Element	E_{4f} (eV)	$\langle R_{4f}\rangle$ (Å)
59	Pr	−14.97	0.526
60	Nd	−16.33	0.504
61	Pm	−17.14	0.486
62	Sm	−18.23	0.467
63	Eu	−19.32	0.451
65	Tb	−19.05	0.429
66	Dy	−19.05	0.418
67	Ho	−19.32	0.407
68	Er	−19.32	0.398
69	Tm	−19.59	0.389
70	Yb	−19.86	0.379

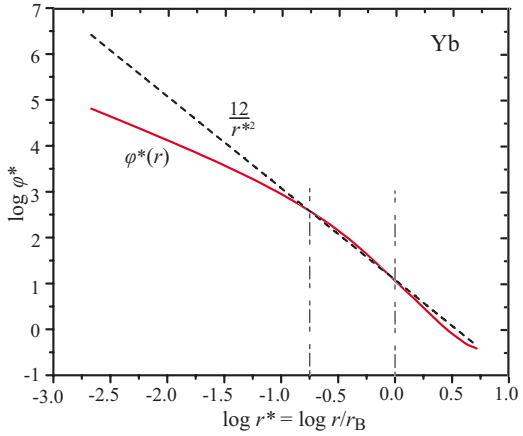

FIG. 4. (Color online) Comparison between $\varphi^*(r^*)$ (Ref. 19) and suggested simple relation $\varphi^*=12/r^{*2}$ for Yb. $\varphi^*(r^*)$ is approximated by $12/r^{*2}$ for $r_B/2 \leqslant r \leqslant r_B$.

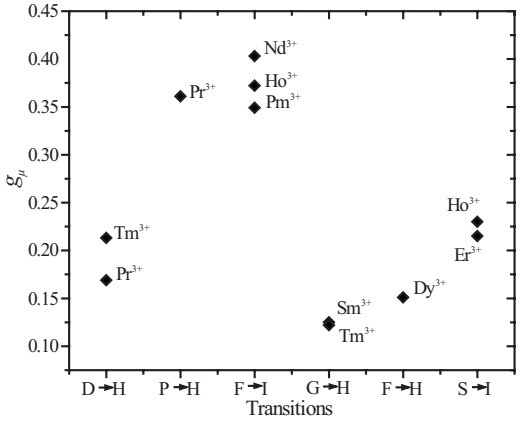

FIG. 5. The dipole factor g_μ values for different rare-earth ions, with different initial and final electronic states. Transitions between similar sets of initial and final states have g_μ values close to each other, showing dependence of g_μ on the initial and final state wave functions.

configuration for that atom in crystals, the larger the average a_n. In general, $a_n=a_n(E_e)$, and $a_n^2(E_{e,1})<a_n^2(E_{e,2})$, for $E_{e,1}<E_{e,2}$ within an f band. We assume the ground state to be composed of the lowest-energy state and take $a_n^2\approx 1$. This allows us to approximate the wave function of the $4f$ electron in crystals by an atom-like wave function.

The atom-like wave functions of $4f$ electrons for the rare-earth ions have been calculated numerically by solving the Hartree–Fock–Slater equation and using the self-consistent field method,[18] which is expressed as

$$\left[-\frac{\mathrm{d}^2}{\mathrm{d}r^{*2}}+\frac{l(l+1)}{r^{*2}}+\varphi^*(r)\right]P_{nl}(r)=E_{nl}^*P_{nl}(r),$$

$$P_{nl}(r)=\frac{1}{4\pi}\int_0^{2\pi}\int_0^{\pi} r\psi_{nl}^o(\boldsymbol{r})\sin\theta\,\mathrm{d}\theta\,\mathrm{d}\phi. \tag{28}$$

From this, the total energy of $4f$ electrons is found and is given in Table I.

To estimate $\mu_{ph\text{-}e}$ from the energy eigenvalues listed in Table I, we examine the definition of the transition dipole moment

$$\boldsymbol{\mu}_{ph\text{-}e}=\int \psi_f^* e_c \mathbf{x}\psi_i \mathrm{d}V. \tag{29}$$

The transition dipole moment $\boldsymbol{\mu}_{ph\text{-}e}$ is approximated as electronic charge times the net displacement $\Delta R_{e,if}$ of the optically active electron during the transition, or

$$|\boldsymbol{\mu}_{ph\text{-}e}|\simeq g_\mu e_c \Delta R_{e,if}, \tag{30}$$

where g_μ is a dipole factor which depends on the shapes of the wave functions (initial and final states) and a_n is a measure of atom-like behavior of the $4f$ electron in the condensed state.

In the neighborhood of the average $4f$ electron radius $\langle R_{4f}\rangle$, we can approximate the potential function $\varphi^*(r)\simeq l(l+1)/r^{*2}$ (Fig. 4) for all rare-earth elements of interest. Here,

TABLE II. Radial charge displacement ΔR_e estimates and corresponding g_μ values for some rare-earth elements doped in LaF_3 crystal, calculated using μ_{ph-e} from Table IV.

z	Element	Transition	$\Delta E_{e,g}$ (eV)	ΔR_e (Å)	$e_c\Delta R_e$ (C m)	g_μ
59	Pr^{3+}	$^1D_2\rightarrow{}^3H_4$	2.07	0.034	5.44×10^{-31}	0.17
		$^3P_0\rightarrow{}^3H_4$	2.53	0.041	6.56×10^{-31}	0.36
60	Nd^{3+}	$^4F_{3/2}\rightarrow{}^4I_{9/2}$	1.41	0.020	3.20×10^{-31}	0.40
61	Pm^{3+}	$^5F_1\rightarrow{}^5I_4$	1.52	0.020	3.20×10^{-31}	0.35
62	Sm^{3+}	$^4G_{5/2}\rightarrow{}^6H_{5/2}$	2.22	0.027	4.32×10^{-31}	0.13
66	Dy^{3+}	$^4F_{9/2}\rightarrow{}^6H_{15/2}$	2.60	0.027	4.32×10^{-31}	0.15
67	Ho^{3+}	$^5S_2\rightarrow{}^5I_8$	2.27	0.023	3.68×10^{-31}	0.23
		$^5F_5\rightarrow{}^5I_8$	1.91	0.019	3.04×10^{-31}	0.37
68	Er^{3+}	$^4S_{3/2}\rightarrow{}^4I_{15/2}$	2.27	0.022	3.52×10^{-31}	0.22
69	Tm^{3+}	$^1D_2\rightarrow{}^3H_6$	3.46	0.033	5.28×10^{-31}	0.21
69	Tm^{3+}	$^1G_4\rightarrow{}^3H_6$	2.63	0.025	4.00×10^{-31}	0.12

TABLE III. Values of B_i in the Judd–Ofelt transition dipole moment relation for some rare-earth ion in LaF_3 (Ref. 23).

Ion	$B_2\times10^{-20}$ (cm^2)	$B_4\times10^{-20}$ (cm^2)	$B_6\times10^{-20}$ (cm^2)
Nd^{3+}	0.35	2.57	2.50
Eu^{3+}	1.19	1.16	0.39
Tb^{3+}	1.1	1.4	0.9
Ho^{3+}	1.16	1.38	0.88
Er^{3+}	1.07	0.28	0.63
Tm^{3+}	0.52	0.59	0.22

potential function $\varphi^*(r)=2m_e r_B^2\varphi(r)/\hbar^2$, $E^*=2m_e r_B^2 E/\hbar^2$, and $r^*=r/r_B$ is a dimensionless parameter, where the r_B is the Bohr radius. Then we write the dimensionless transition energy as

$$\Delta E^*_{e,g}=E^*_{e,f}-E^*_{e,i}=\frac{1}{2}[\varphi^*(R_{e,i})-\varphi^*(R_{e,f})]\simeq 6\left(\frac{1}{R^{*2}_{e,i}}-\frac{1}{R^{*2}_{e,f}}\right)$$

$$E_{e,f}+E_{e,i}\simeq 2E_{4f}$$

$$\frac{1}{R^{*2}_{e,i}}+\frac{1}{R^{*2}_{e,f}}\simeq 2\frac{1}{R^{*2}_{4f}}. \tag{31}$$

We assume $E_{e,f}+E_{e,i}\approx 2E_{4f}$, to estimate $\Delta R_e=R_f-R_i$. Table I lists ΔR_e and g_μ, estimated for the rare-earth ions doped in the LaF_3 crystal. Figure 5 shows that the g_μ values for a particular transition between similar set of initial and final states are close. Table II lists the values of g_μ for the various rare-earth ions with different initial and final states. The magnitude of g_μ for a transition between similar states is expected to be higher than for transitions between dissimilar states, due to a better overlap between the spherical harmonics of initial and final states in Eq. (29). For example, g_μ for an $^2F_{5/2}$ to $^2F_{7/2}$ transition in Yb is expected to be higher than any other transitions in rare-earth ions. For Yb^{3+} in CaF_2 crystal, $e_c\Delta R_e$ is estimated as 1.75×10^{-31} C m, which is nearly the same as the experimental value of 1.81×10^{-31} C m, which means an $F\rightarrow F$ transition should also have a high value of g_μ.

B. Judd-Ofelt theory estimation of transition dipole moment

Judd–Ofelt theory gives an accurate estimation of transition dipole moment with minimal experimental input, and $\mu_{ph\text{-}e}$ is determined by the dipole approximation[20]

$$\mu^2_{ph\text{-}e}=\frac{1}{(2J+1)}[\chi\bar{F}^2+n\bar{M}^2], \tag{32}$$

where $\bar{F}^2$ and $\bar{M}^2$ represent the matrix elements of the electric and magnetic dipole operators, respectively, joining an initial state J to the final state J', i.e., $^{2S+1}L_J\rightarrow{}^{2S'+1}L'_{J'}$, $\chi=(n^2+2)^2/9n$, and n is the refractive index of the medium. The factor $2J+1$ is added, since the matrix elements of μ_e are summed over all components of the initial state i. Since the photon-induced electron transition is electric in nature, we will only discuss $\bar{F}^2$ component.

The transition dipole moment of induced electric dipole transition within the f^n shell configuration is independently derived by Judd and Ofelt and is known as the Judd–Ofelt theory.[21] Judd–Ofelt theory uses semiempirical data to find the various atomic parameters of the rare-earth (trivalent lanthandes) ions. $\bar{F}^2$ matrix element is expanded as $\bar{F}^2=e_c^2\Sigma_{i=2,4,6}B_i\langle\psi J|U^{(i)}|\psi' J'\rangle^2$ to give the transition dipole moment as

$$\mu^2_{ph\text{-}e}=\frac{1}{(2J+1)}\frac{(n^2+2)^2}{9n}e_c^2\sum_{i=2,4,6}B_i\langle\psi J|U^{(i)}|\psi' J'\rangle^2, \tag{33}$$

where B_i is the crystal field parameter given in Table III and $U^{(i)}$ is a unit tensor operator of rank i where $i=2,4,6$. The crystal parameter B_i is defined by $B_i=(2i+1)\Sigma_k|D_k|^2(2k+1)^{-1}I^2(k,i)$, where D_k (k odd) are the odd-parity terms in the static crystal field expansion and $I^2(k,i)$ contain integrals involving the radial parts of the $4f^n$ wave functions, the excited opposite-parity electronic-state wave functions, and the energy separating these states.[22] The matrix element $\langle\psi J|U^{(i)}|\psi' J'\rangle^2$ does not vary with the host; therefore, the value calculated in Ref. 23 can be used for most of the electronic transition of the rare-earth ions. Using the above relationship, the radiative lifetimes and the electric dipole moment are calculated for rare-earth ions in LaF_3 crystal as listed in Table IV.

TABLE IV. Calculated values of radiative lifetime and electric dipole moment for some rare-earth ions in LaF_3 crystal (Ref. 23). The index of refraction n is between 1.57 and 1.65.

Ion	Transition	$\Delta E_{e,g}$ (cm^{-1})	$\langle\psi J\|U^{(2)}\|\psi' J'\rangle^2$	$\langle\|U^{(4)}\|\rangle^2$	$\langle\|U^{(6)}\|\rangle^2$	τ_r (μs)	μ_e (C m)
Nd^{3+}	$^4F_{3/2}\rightarrow{}^4I_{9/2}$	11386	0.0000	0.2283	0.0554	635	1.31×10^{-31}
Tb^{3+}	$^5D_3\rightarrow{}^7F_6$	4294	0.0000	0.2323	0.4129	809	4.98×10^{-32}
Ho^{3+}	$^5F_5\rightarrow{}^5I_8$	11137	0.0000	0.0102	0.0930	778	1.14×10^{-31}
Er^{3+}	$^4S_{3/2}\rightarrow{}^4I_{15/2}$	22495	0.0000	0.0000	0.1255	1020	7.67×10^{-32}
Tm^{3+}	$^1D_2\rightarrow{}^3H_6$	15027	0.0000	0.0000	0.2550	137	1.12×10^{-31}
Tm^{3+}	$^1G_4\rightarrow{}^3H_6$	5675	0.5395	0.7261	0.2421	1560	4.93×10^{-32}

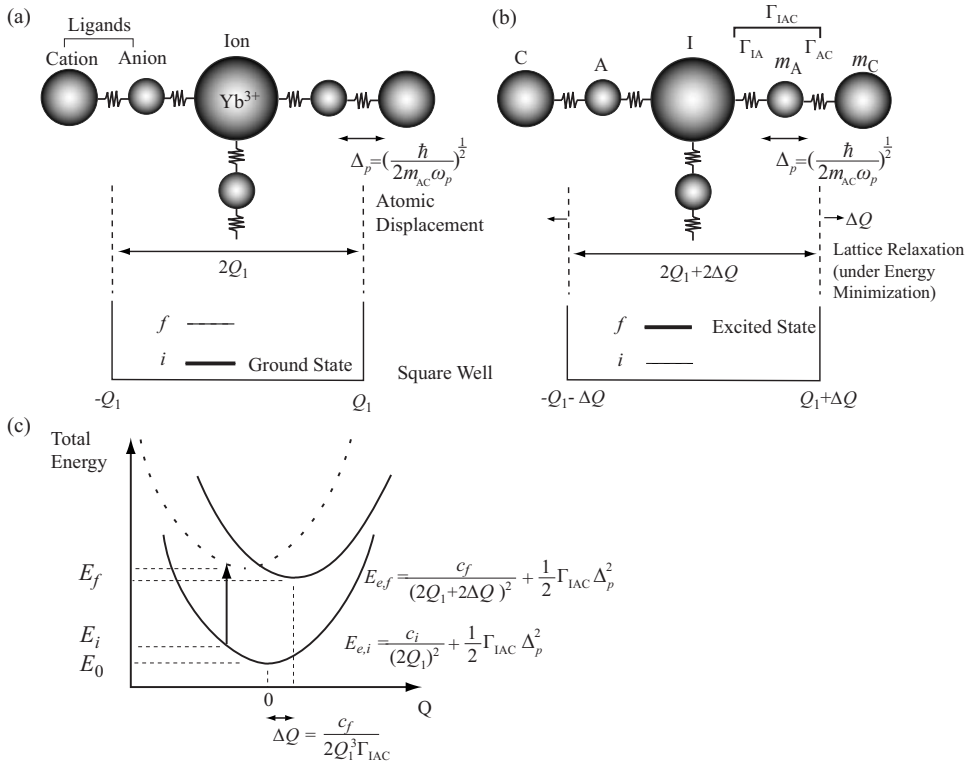

FIG. 6. Variation of electron energy with respect to the normal coordinate, at the doped-ion site, using an infinite square well model. (a) Ground state and (b) excited state. (c) The configuration coordinate diagram for the process.

III. ELECTRON-LATTICE INTERACTION FOR OPTICAL PHONON

Electron-phonon interaction involves several physical parameters which characterize its strength. The electron-phonon coupling is defined using a simplified defect model at the ion site, and the available phonon density of states is estimated using the Debye-Gaussian model.

A. Electron-phonon coupling

Electron-phonon coupling is analogous to the deformation potential theory in semiconductors; however, the domain modification is necessary, due to the discrete state nature of the bound electrons. For example, while semiconductor deformation potential is defined within the boundary of a unit cell, the electron-phonon coupling potential is here defined at the doped ion site.

We adapt a defect model to estimate the electron-phonon coupling potential using electrons in an infinite square well. The solution is not exact; however, this interpretation provides the physical picture of the electron-phonon coupling for different host materials.[24] The doped ion is treated as a defect site surrounded by an infinite potential. Although the electron experiences potential by the nucleus of the doped ion, this is neglected when comparing electrons in different host materials; thus, the interaction potential is not an absolute value, but a relative one which varies for different host constituents. Figure 6(a) shows the electron trapped in an infinite square well of width $2Q_1$. The equilibrium bond lengths are determined by the intermolecular forces and the structure of the molecular complex, estimated from the structural metrics.[25] The peak stretching mode frequency is estimated using the combinative rule given as

$$\Gamma_{AC} = g_s(\Gamma_{AA}\Gamma_{CC})^{1/2}, \tag{34}$$

where g_s is a structural parameter which depends on the crystal structure, and Γ_{AC} is the estimated force constant between anion and cation, using the monatomic force constants Γ_{AA} and Γ_{CC}. Figure 6(b) shows that electron in an infinite square well at the excited state. Figure 6(c) shows the configuration coordinate diagram for the two states.

Estimated magnitudes of g_s, for some related crystals, are listed in Table V. Satisfactory results have been reported in Ref. 26, using these estimates. The estimated peak phonon frequency, for some elements, is plotted in Fig. 7, for C-F crystal, where C is the cation element. As shown in the figure, the Periodic Table first column alkali metals tend to have a lower peak energy. Generally, trend follows the Periodic Table row, indicating relation to the outer most electronic configuration of the cation. This relation is not pursued further here. For the remainder of the analysis, these phonon peaks are assumed as the most probable phonon energies in the coupling with electron of the ion, at moderate temperatures. Figure 8 shows the variation of g_s with respect to the atomic number and some crystal structure groups are identified. No particular trend is found; however, all g_s values are in the 0.2–0.5 range.

The ground-state energy of the electron in Fig. 6(a) is

TABLE V. Magnitude of structural parameter g_s for some crystalline solids.

Structure	Host	g_s
Cubic	CdF_2	0.30
	AlF_3	0.33
	LiF	0.23
	LiCl	0.36
Tetragonal	MgF_2	0.35
	MnF_2	0.31
	NiF_2	0.27
	PbF_2	0.23
	TlF	0.48
Octahedra	Fe_3O_4	0.20
Trigonal	CeF_3	0.23
	InF_3	0.42
	LaF_3	0.31
	$FeCl_2$	0.44
	VF_3	0.38
Monoclinic	SnF_2	0.38
	$ZrCl_4$	0.54
	$IrCl_3$	0.40
Orthorhombic	SbF_3	0.43
	VF_4	0.41

$$E_{i,1} = \frac{c_i}{(2Q_1)^2} + \frac{1}{2}\Gamma_{\mathrm{IAC}}\Delta_p^2, \quad \Delta_p = \left(\frac{\hbar}{2m_{\mathrm{AC}}\omega_{p,p}}\right)^{1/2}, \quad (35)$$

where c_i is a constant that depends on the state quantum number and is independent of the bond, Γ_{IAC} is the effective force constant of the ion-anion-cation set, Δ_p is the displacement of the anion, due to a phonon with frequency $\omega_{p,p}$, and m_{AC} is the effective mass of the anion-cation pair.

The excited state energy of the electron in Fig. 6(b) is

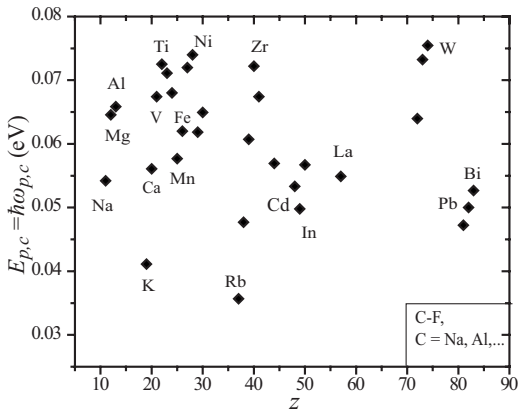

FIG. 7. (a) Peak stretching mode frequency using diatomic molecular data for cation-fluoride pair.

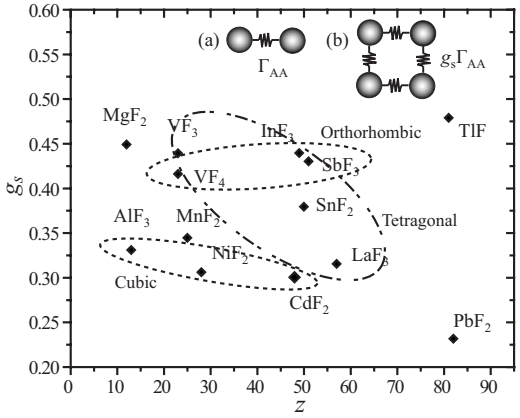

FIG. 8. Variation of the structural parameter g_s with respect to the atomic number, identifying some crystal structure grouping. The results are for C-F where C is the cation as shown.

$$E_f = \frac{c_f}{(2Q_1 + 2\Delta Q)^2} + \frac{1}{2}\Gamma_{\mathrm{IAC}}\Delta_p^2. \quad (36)$$

Since in general $Q_1 \gg \Delta Q$, we expand $(2Q_1+2\Delta Q)^{-2}$ in terms of strain $\Delta Q/Q_1$, i.e.,

$$E_f = \frac{c_f}{(2Q_1)^2} + \frac{1}{2}\Gamma_{\mathrm{IAC}}\left(\Delta_p - \frac{c_f}{2Q_1^3\Gamma_{\mathrm{IAC}}}\right)^2 - \left(\frac{c_f}{2Q_1^3}\right)^2 \frac{1}{2\Gamma_{\mathrm{IAC}}}, \quad (37)$$

where c_f is again independent of the bond. In this treatment, since c_i and c_f are independent of ligands and are only a function of the ion, we compare the magnitude of change in electronic energy in response to ligand (lattice) vibration. In Eq. (37), the electron oscillates about the new equilibrium point $c_f/2Q_1^3\Gamma_{\mathrm{IAC}}$ and its energy is reduced by $(c_f/2Q_1^3)^2(1/2\Gamma_{\mathrm{IAC}})$.

To analyze the electron energy change due to the displacement of the ligands (phonon), a simplified linear-chain model is considered. As discovered in Ref. 14, the most probable mode participating with electron of the ion is the breathing mode of the isolated ion-ligand complex. When considering the local available modes in the vicinity of the ion, stretching mode of the anion-cation pair is important.[16] Then from these structural metrics, the peak frequency, $\omega_{p,p}$, and the cut-off frequency, $\omega_{p,c}$, are estimated as

$$\omega_{p,p} = \left(\frac{g_s\Gamma_{\mathrm{AC}}}{m_{\mathrm{AC}}}\right)^{1/2}, \quad \omega_{p,c} = \left(\frac{2g_s\Gamma_{\mathrm{AC}}}{m_{\mathrm{AC}}}\right)^{1/2}. \quad (38)$$

Due to the lattice vibration, the electron will oscillate as a harmonic oscillator which is displaced by Δ_p. Δ_p is a function of m_{AC} and $\omega_{p,p}$. Then using the following energy of the harmonic oscillator, the electron-phonon coupling (the rate of electronic energy change due to displacement of normal coordinates) is defined as

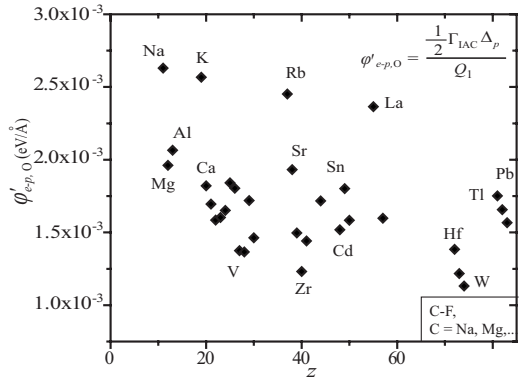

FIG. 9. Partial electron-optical phonon interaction potential using the infinite-square-well model for cation-fluoride pair.

$$\varphi'_{e\text{-}p,\mathrm{O}} \equiv \frac{\frac{1}{2}\Gamma_{\mathrm{IAC}}\Delta_p^2}{Q_1}, \quad E_{e\text{-}p} = \frac{1}{2}\Gamma_{\mathrm{IAC}}\Delta_p^2. \tag{39}$$

For simplicity, a linear derivative of the potential with respect to the normal coordinates is assumed. We have used the effective ion-anion-cation force constant as a component to represent the change in the energy of the ion electron. This is because the lattice is not composed of independent springs (as shown in the failure of the Einstein heat capacity model[27]). Figure 9 shows the calculated interaction potential using the square well model, for various atoms in C-F, where C is the cation. The domain of the interaction is selected as two atomic spacings extending in the direction of the linear chain. Unlike semiconductors, for doped ion the electrons of the rare-earth elements are highly localized within one or two atomic spacings.[28] Thus, it is reasonable to consider only the short-range interaction of the electron with the optical phonons. Figure 9 shows that the coupling is a slow decreasing function of the atomic number z.

Preliminary *ab initio* calculations of the electron-phonon coupling in Yb^{3+}:Cd-F were conducted using WIEN2K, to confirm the current hypothesis.[29] The discrete energy levels of the Yb^{3+}:Cd-F was calculated using the electron band structure near the gamma point. The equilibrium structure energy level was first plotted and compared with the non-equilibrium (under longitudinal fluorine atom displacement) energy levels to estimate the electronic energy change due to longitudinal optical phonon mode (modeled as oscillation of fluorine atom). The results show that the electron-phonon coupling is within the uncertainty of the analytical model.

B. Phonon density of states estimation

Fernandez *et al.*[13] used the Debye-Gaussian model for the phonon density of states (DOS), which is close to the Debye model at low energies and has a Gaussian distribution at the center of the phonon spectrum, i.e.,

$$D_p(E_p) = c_D E_p^2 \exp\left[-\left(\frac{E_p - E_{p,t}}{\Delta E_p}\right)^2\right]. \tag{40}$$

Here, E_p is the phonon energy, $E_{p,t}$ is the central frequency, ΔE_p is the width of the phonon spectrum estimated to be approximately 0.012 39 eV, and c_D is a normalization constant. To find the normalization constant, we integrate the phonon DOS from zero to $E_{p,c}$ (the cut-off phonon energy). Such an approximation is useful for scaling D_p in mixed glasses, where the structure is not known and the exact density of states is difficult to calculate. We use this approximation to estimate D_p of the host material. The cut-off frequencies calculated in Sec. III A are used to estimate the total DOS of the bulk materials. Comparison among prediction by Eq. (40), prediction by MD simulation for Y_2O_3,[14] and experimental result for Fe_3O_4 (Ref. 30) are shown in Figs. 10(a) and 10(b). There are general agreement with both MD predictions and the experimental results. However, since the frequency estimate uses the anion-cation pair, only the second peak is estimated and the first and third peaks which are likely due to cation-cation and anion-anion oscillations cannot be predicted using Eq. (40). In the interaction domain (in the vicinity of the rare-earth ion), only cation-anion pairs are relevant, due to absence of anion-anion and cation-cation oscillating pairs. The predicted peak and cut-off frequency are compared with the calculated values using the normal mode frequencies of the host complexes and these are listed in Table VI.

The frequency estimation is compared with an analytic normal mode calculation using the interatomic potentials between the cation and anion, i.e.,

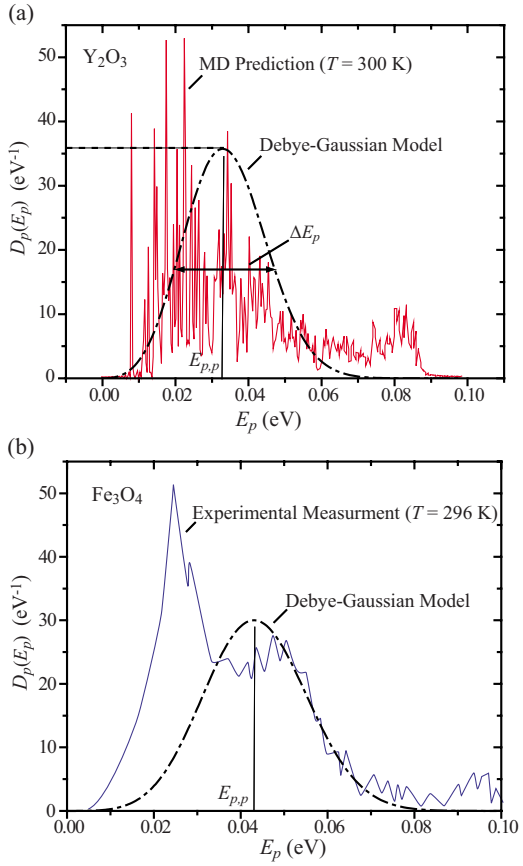

FIG. 10. (Color online) (a) Comparison between the MD simulation phonon DOS (Ref. 14) and the Debye-Gaussian model, for Y_2O_3. (b) Comparison between the experimental results (Ref. 30) for phonon DOS and the Debye–Gaussian model, for Fe_3O_4.

TABLE VI. Comparison of the phonon DOS peak energy $E_{p,p}$ values using the linear-chain model, with the ion-ligand complex, and the experimental values for some diatomic crystals.

	Linear chain	Complex	Expt.
C-F	$E_{p,p}$ (eV)	$E_{p,p}$ (eV)	$E_{p,p}$
Cd-F	0.0533	0.0421	0.0459
Cd-Cl	0.0302	0.0310	0.0310
Zr-F	0.0722		0.0719
In-F	0.0498		0.0632

$$\Gamma \approx \Gamma_{\mathrm{IA}} + 4\Gamma_{\mathrm{IA}} \quad \text{for IA}_6 \text{ type coordination},$$

$$\Gamma \approx \Gamma_{\mathrm{IA}} + 2\Gamma_{\mathrm{AA}} \quad \text{for IA}_8 \text{ type coordination},$$

$$E_{p,p} = \hbar\left(\frac{\Gamma}{m_{\mathrm{A}}}\right)^{1/2} \quad \text{for the breathing mode} A_{1g}. \tag{41}$$

The peak phonon energy of the DOS, $E_{p,p}$, is assumed to coincide with the breathing mode frequency and is related to the central phonon energy, $E_{p,t}$, by

$$E_{p,p} = E_{p,t} - \frac{\Delta E^2}{E_{p,t}}. \tag{42}$$

Since the breathing mode frequency follows $E_{p,A_{1g}} \propto m_{\mathrm{A}}^{-1/2}$, the population of the high-energy phonons decreases for the choice of a lighter anion. For CNBZn glass, $E_{p,p,\mathrm{CdF_2}} \simeq 0.0421$ eV and using $E_{p,A_{1g}} \propto m_{\mathrm{A}}^{-1/2}$, $E_{p,p,\mathrm{CdCl_2}}$ is estimated as 0.0310 eV, which matches well with the Cd-F (0.0459 eV) and Cd-Cl (0.0310 eV) observed vibrations.[31] ΔE can be approximated as the difference in peaks of the Cd-F and Cd-Cl vibrations; therefore, $\Delta E \simeq 0.0149$ eV, which is close to $\Delta E \simeq 0.0124$ eV suggested by Fernandez *et al.*[13]

IV. COOLING RATE

A. Optimal photon frequency

As discussed in Sec. I, the input off-resonance photon frequency determines the frequency of the phonon required to excite the electron from ground state. In turn, the input photon can be varied according to the distribution of the available phonon frequency in the lattice. By using the approximations made in Sec. III and using Eq. (19), we write the cooling rate as

$$\frac{\dot{S}_{ph\text{-}e\text{-}p}}{Q_{ph,i}} = \frac{\pi\hbar}{2\epsilon_{\mathrm{o}} m_{\mathrm{AC}}} \langle \mu_{ph\text{-}e} \rangle^2 \varphi'^2_{e\text{-}p,\mathrm{O}} \frac{D_p(E_p) f_p^{\mathrm{o}}(E_p)}{E_p^3} \frac{\hbar\omega_{ph,i} n_d L}{u_{ph}} \times \left(1 - \frac{\bar{\omega}_{ph,e}}{\omega_{ph,i}} \eta_{e\text{-}ph}\right). \tag{43}$$

The cooling rate is plotted in Fig. 11(a) by taking into account the multiple simultaneous transitions from the excited manifold of Yb^{3+} to the four ground-state manifolds.[32] Then Eq. (43) becomes

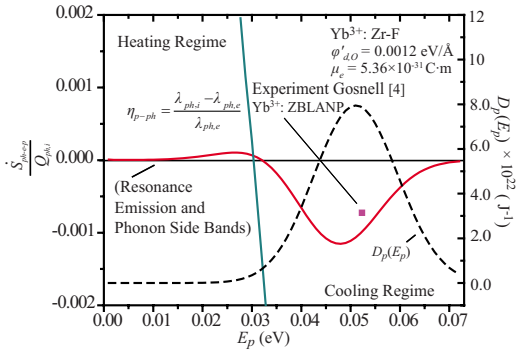

FIG. 11. (Color online) (a) Idealized (resonance) and a realistic (side bands) normalized cooling rate as a function of phonon energy, for Yb^{3+}: Zr-F. The cooling efficiencies are also plotted as solid line. The experimental result (Ref. 6) is also shown.

$$\frac{\dot{S}_{ph\text{-}e\text{-}p}}{Q_{ph,i}} = \sum_{k=0,1,2,3} \frac{\pi\hbar}{2\epsilon_{\mathrm{o}} m_{\mathrm{AC}}} \langle \mu_{ph\text{-}e} \rangle^2 \varphi'^2_{e\text{-}p,\mathrm{O}} \times \frac{D_p(E_p) f_p^{\mathrm{o}}(E_p)}{E_p^3} \frac{\hbar\omega_{ph,i} n_d L}{u_{ph}} \left(1 - \frac{\omega_{ph,e,k}}{\omega_{ph,i}} \eta_{e\text{-}ph}\right), \tag{44}$$

where $j=0,1,2,3$ represents resonance, first, second, and third phonon side bands, respectively. The results shows that the maximum cooling rate is to the left of the phonon peak. This is due to the phonon distribution function which suppresses phonons with higher energy and significantly influences the cooling rate at low temperatures.

Figure 12 shows distribution of the maximum cooling rate as a function of the atomic number. The trend is fitted to a fourth-order polynomial to guide the eyes. The results show that there are two peaks, between atomic numbers 20 and 30 and 75 and 85. This trend supports the recent successes of blending of light and heavy cations as host materials for laser cooling of solids. However, as the temperature decreases and the available high-energy phonons diminish rapidly (Bose–

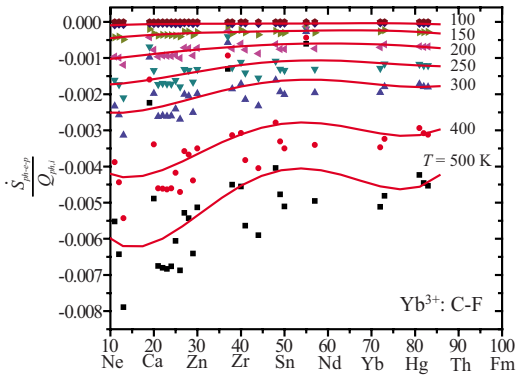

FIG. 12. (Color online) Dimensionless cooling rate as a function of atomic number, for discrete values of temperature for Yb^{3+}: C-F where C stands for cation. Some elements are added for reference. Also, a fourth-order polynomial fit is shown to guide the eyes. Note that semiconductors and rare-earth materials have been omitted.

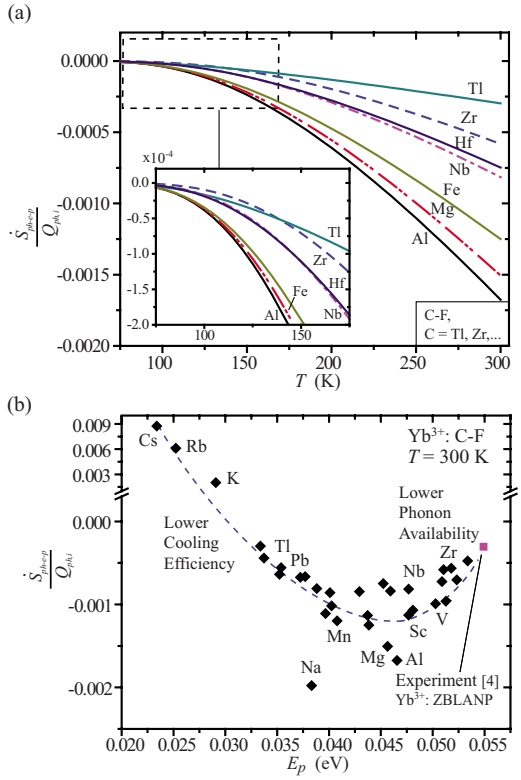

FIG. 13. (Color online) (a) Dimensionless cooling rate as a function of temperature, for Yb^{3+}: Tl-F, Zr-F, Hf-F, Nb-F, Fe-F, Mg-F, and Al-F. The results are for ideal conditions, i.e., quantum efficiency of one and identical fcc structures. (b) The maximum, normalized cooling rate for various cation-fluoride pairs, as function of phonon energy for Yb^{3+}: C-F. Note that semiconductors and rare-earth materials have been omitted. The dashed line is only intended to guide the eyes.

Einstein distribution f_p^0), the cooling rate is quickly suppressed.

B. Optimal host pairs

The above analysis provides a guide to the selection of ion-host materials for optimal performance. Here we compare various host materials, based on performance by atomic pairs, and we choose F as one of the atoms. Figure 13(a) shows variation of dimensionless cooling rate with respect to temperature, for some C-F pairs with Yb^{3+} ion. The crystal structure assumed is fcc, which has C-F pairs as the ion immediate ligands. Here C is Tl, Zr, Hf, Nb Fe, Mg, and Al. These structures may not be realized, for example, AlF_3 is an stable, existing compound. However, if a blend of different C-F pairs are made, the contributions of these pair ligands exist at the ion site. Figure 13(a) shows that Al, which has relatively low phonon peak energy predicted by Fig. 11, exhibits high cooling rate over a wide range of temperatures; however, one can expect that the energy removed per transition is low (low capacity). On the contrary, one can expect the energy removed per transition is high (high capacity) for Zr (due to relatively high phonon peak energy), yet the performance decreases rapidly as the temperature decreases.

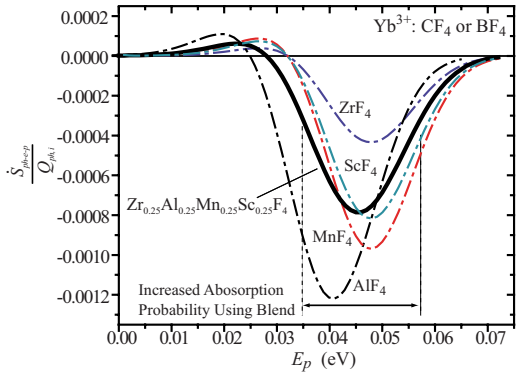

FIG. 14. (Color online) Dimensionless cooling rate as a function of phonon energy for diatomic host Yb^{3+}: CF_4 or blend host, BF_4. The cooling rates have been calculated using ideal conditions, i.e., quantum efficiency of 1 and fcc structure, and are linearly superimposed. Although the magnitude of the cooling rate is moderated, the absorption probability increases as the phonon spectrum broadens. The cooling rates for diatomic hosts are shown in dashed lines and exhibit less broadening.

The inset in Fig. 13(a) shows that at temperatures near 150 K, it is possible to reach even lower temperature with Tl compared to Zr.

The maximum cooling rate, for some cation-fluoride pairs, is given in Fig. 13(b). The results show that the first column alkali metals from the Periodic Table are not good candidates for laser cooling at $T=300$ K. However, due to the relatively lower phonon energy, these elements are expected to be more suitable at lower temperatures with the exception of Cs and Rb. The results are expected from Eq. (44), which shows that there are several competing processes in laser cooling of solids. These are the following: (a) higher phonon peak energy results in more energy removed per transition, (b) lower phonon peak energy results in higher phonon distribution values, (c) low cut-off frequency results in higher phonon density of states, and (d) higher cut-off frequency results in higher a nonradiative decay.

Using the above discussions, it is possible to quantitatively predict the cooling performance of a blended material. Figure 14 shows the cooling performance of an example blend of host materials. In practice, the composition discussed here may not be realized; however, the blend here provides an example providing a valuable general guide. The figure shows that blending materials which have different phonon peak energies increases the half width of the transition. This, in turn, increases the transition probability. One can expect that as the half width broadens, it increases the probability of various phonon modes available in the lattice coupling with the electron in oscillation. This blending strategy is expected to increase the absorption rate as much as a factor of 2.

Results of Figs. 13(a) and 14 suggest using elements Al, Mn, Na, and Mg in the host blend. Nevertheless, for optimized cooling performance, wide range of elements should be present in the blend for increased absorption probability (with the exception of Rb and Cs).

V. DISCUSSION

A. Transition dipole moment optimization

While selecting the dopant ion for a large $\mu_{ph\text{-}e}$, according to the charge-displacement estimation model, the following general guidelines apply. First, a large energy gap $\Delta E_{e,g}$ would result in higher $\Delta R_{e,if}$ and, therefore, larger $\mu_{ph\text{-}e}$. However, a large $\Delta E_{e,g}$ also results in a lower cooling efficiency for the overall laser cooling process. A small energy gap, on the other hand, would lead to high nonradiative decay.

Secondly, a transition between similar states, for example, ${}^2F_{5/2} \rightarrow {}^2F_{7/2}$, leads to a larger g_μ, and, therefore, a larger $\mu_{ph\text{-}e}$. The excited state chosen for the transition should have the same total angular momentum as the ground state of the ion.

Lastly, the energy levels for the transition should be selected in a manner such that there are no allowed energy levels in between the ground and the excited state manifolds, which can result in nonradiative decay that severely affects the cooling efficiency. For example, the radiative lifetime of ${}^4I_{9/2}$ state of Er^{3+} is computed to be 20.7 ms, but its observed value is 0.15 ms,[23] as a result of the nonradiative decay due to the presence of intermediate levels between ${}^4I_{9/2}$ and the ground state ${}^4I_{15/2}$.

The calculated energy levels of various rare-earth ions are presented in Ref. 33. Ce, Pr, Nd, Pm, Sm, Eu, Tb, and Dy have energy gaps between the ground state and the lowest excited state, with magnitudes less than $2k_BT$ (at room temperature). This would lead to high rates of nonradiative decay. Gd has a very large energy gap between the ground and the lowest excited state, which would result in a low laser cooling efficiency. Also, the ground and excited states have different L values; therefore, a transition between these states would have a low value of g_μ. Ho, Er, Tm, and Yb have ground and excited states with the same total angular momentum L. Amongst these, Yb has the largest energy gap $\Delta E_{e,g}$ between the ground and the lowest excited state, and should result in high $\Delta R_{e,if}$ and low nonradiative decay.

B. Limits in laser cooling of solids

Figure 15(a) shows a qualitative prediction of the cooling rate when the phonon limit is removed. The results show that the maximum off-resonance absorption and the maximum anti-Stokes cooling will occur when the maximum normal mode of the complex coincides with the peak of a single available mode, i.e., all of the available phonon modes are at the cut-off frequency. This is a hypothetical case since the integral of phonon DOS at the cut-off frequency has to be unity (a delta function) meaning there is no other phonon mode present (except for the phonon modes corresponding to the cut-off frequency). This will increase the phonon DOS by approximately a factor of 10. Note that when the limit from the structure (multiple phonon energy) is lifted, the absorption limit becomes only a function of the phonon distribution function $f_p^o(T)$. Figure 15(b) shows that when multiple-pair blends are used as hosts and low symmetry is achieved at the ion site, multiple cooling peaks are possible. Multiple-pair blends provides multiple phonon DOS peaks which can span across the phonon spectrum. When low symmetry is present at the ion site, the normal mode of the complex becomes broader, allowing multiple phonon mode couplings.

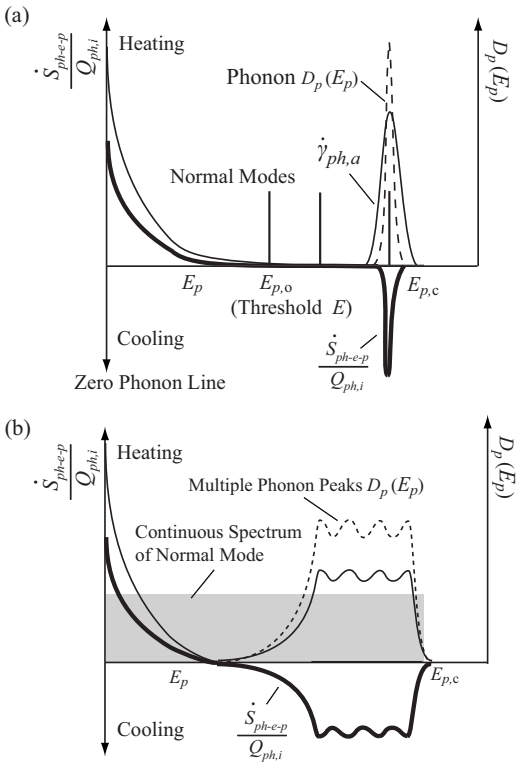

FIG. 15. (a) Variation of dimensionless cooling rate, absorption rate, and phonon DOS with respect to phonon energy. Maximum cooling rate can be achieved when the energy of maximum normal mode of the ion-ligand complex coincides with the cut-off phonon energy $E_{p,c}$ of the host and is the most available mode. (b) Multiple cooling peaks (increased cooling probabilities) are possible when multiple blends are present in the host and low symmetry is achieved at the ion site.

C. Off-resonance transition dipole moment

The structural metrics which are developed above suggest multiple improvements and explain recent experimental success of laser cooling of blend solids. However, to scale various blended host material and doped ions, direct comparison amongst various photon-electron-phonon interaction terms is necessary. We use Eq. (19) to define an a effective transition dipole moment which is analogous to the transition probability (Einstein coefficient A) when phonon participation is present, i.e.,

$$\dot{\gamma}_{ph\text{-}e\text{-}p} = \frac{1}{\tau_{ph\text{-}e\text{-}p}} = \frac{\omega_{e,g}^3}{3\pi\epsilon_o\hbar u_{ph}^3} \frac{3\pi^2\hbar^2 u_{ph}^3 \hbar\omega_{ph,i}}{2m_{AC}\omega_{e,g}^3 V} \frac{\varphi'_{e\text{-}p,O} D_p(E_p) f_p^o(E_p)}{E_p^3} \times \langle \mu_{ph\text{-}e} \rangle^2 \equiv \frac{\omega_{e,g}^3}{3\pi\epsilon_o\hbar u_{ph}^3} \mu_{ph\text{-}e\text{-}p}^2, \quad (45)$$

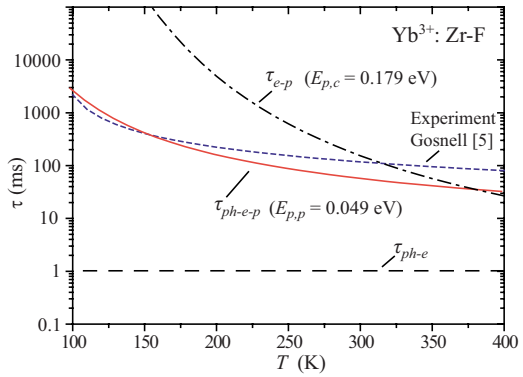

FIG. 16. (Color online) Variation of time constants as a function of temperature. The radiative relaxation time is the shortest followed by the phonon-assisted, photon absorption at low temperatures. Multiphonon relaxation exhibits strong temperature dependence and is dominant at high temperatures.

where $\mu^2_{ph\text{-}e\text{-}p}$ is the phonon-assisted transition dipole moment. This effective transition dipole moment gives the strength of phonon-assisted transition probability for material selection and is directly comparable to the resonance transition dipole moment $\mu_{ph\text{-}e}$.

D. Time scales for laser cooling of solids

As mentioned in Sec. I, laser cooling has three processes and they are characterized by their time constants, namely, $\tau_{ph\text{-}e}$, $\tau_{e\text{-}p}$, and $\tau_{ph\text{-}e\text{-}p}$. Figure 16 shows the temperature dependence of these time constants. The radiative lifetime stays constant with respect to temperature, while the multiphonon relaxation time is a strong function of temperature. The multiphonon decy process is given by[34]

$$\dot{\gamma}_{e\text{-}p} = \dot{\gamma}_{ph\text{-}e}\left[1 - \frac{\exp(\hbar\omega_{p,c}/k_B T)}{\exp(\hbar\omega_{p,c}/k_B T) - 1}\right]^{N_p}, \quad N_p = \frac{E_{e,g}}{\hbar\omega_{p,c}}. \tag{46}$$

Then using the host selection metrics presented in the preceding sections, Eq. (46) is evaluated. The predicted photon-induced, phonon-assisted transition lifetime is compared with the experimental lifetime of Ref. 6 and is in good agreement.

Then the dimensionless cooling rate is expressed as

$$\frac{\dot{S}_{ph\text{-}e\text{-}p}}{Q_{ph,i}} = n_d V \frac{\tau_{ph,tr}}{\tau_{ph\text{-}e\text{-}p}}\left[1 - \frac{\bar{\omega}_{ph,e}}{\omega_{ph,i}}\frac{\tau^{-1}_{ph\text{-}e}}{\tau^{-1}_{ph\text{-}e} + \tau^{-1}_{e\text{-}p}}\right], \tag{47}$$

where $\tau_{ph\text{-}e}$, $\tau_{e\text{-}p}$, and $\tau_{ph\text{-}e\text{-}p}$ are the radiative, nonradiative, and phonon-assisted transition time constants, respectively, and $\tau_{ph,tr}$ is the photon transit time which is defined by $\tau_{ph,tr}=L/u_{ph}$, where L is the sample length (along the beam). We have neglected the reabsorption of emitted photon since it is estimated to be only 0.005% of the total emission rate.[14] This indicates that unlike energy transport, the energy conversion process is a product of the time constants of the processes. The cooling rate is directly limited by the phonon-assisted absorption process, which has a transition rate 2 orders of magnitude smaller than that of the purely radiative transition.

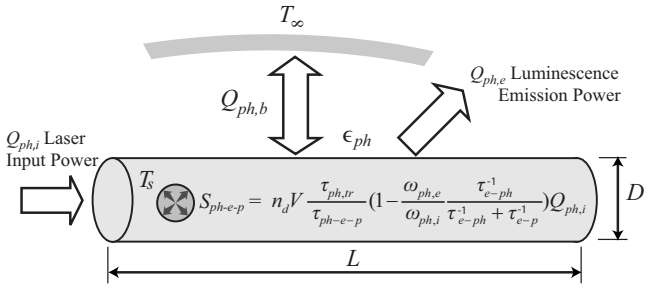

FIG. 17. Heat transfer mechanism of laser cooling of solids. The solid sample exchanges radiation heat with the surroundings through vacuum. The sample temperature will be determined by the balance between the external radiation (thermal load) and the cooling rate.

Figure 16 also suggests that by optimizing the phonon-assisted transition rate, the cooling rate increase by a factor of 2, compared to experiment of Ref. 6, at room temperature.

The sample temperature depends on the balance between the thermal load (radiative heat transfer from surroundings) and the laser cooling rate, shown in Fig. 17. The temperature of the sample is determined from the energy equation

$$Q_{ph\text{-}b} = \dot{S}_{ph\text{-}e\text{-}p}$$

$$\left(\frac{1}{2}\pi D^2 + \pi DL\right)\epsilon_{ph}\sigma_{SB}(T_s^4 - T_\infty^4) = n_d V \frac{\tau_{ph,tr}}{\tau_{ph\text{-}e\text{-}p}}\left(1 - \frac{\bar{\omega}_{ph,e}}{\omega_{ph,i}}\frac{\tau^{-1}_{ph\text{-}e}}{\tau^{-1}_{ph\text{-}e} + \tau^{-1}_{e\text{-}p}}\right)Q_{ph,i}, \tag{48}$$

where ϵ_{ph} is the total emissivity of the sample, σ_{SB} is Stefan–Boltzmann constant, and T_s and T_∞ are the sample and surroundings temperatures. This shows that as the cooling power increases, the thermal load increases rapidly restricting the maximum cooling temperature. With the factor of 2 increase in the cooling rate, a 30% decrease in the T_s is expected, compared to the existing experiment.[6]

Further improvement by photon trapping and possibility of using nanostructures to tailor D_p for improved cooling rate have been discussed in Ref. 14

VI. CONCLUSION

Laser cooling of solids is interpreted as a phonon absorption followed by an off-resonance photon absorption process. The transition dipole moment is expected to be the highest for Yb^{3+}, due to high-energy separation and no intermediate available states between the ground and excited states. The anti-Stokes process is expected to have the highest probability when the normal modes of the ion-ligand complex coincide with the maximum available phonon modes predicted

by the diatomic Debye-Gaussian phonon DOS model. The model predicts that the ideal laser cooling host material varies with target temperature and the model successfully predicts the recent success in using blends of elements for laser cooling of solids. New materials such as Mn, Nb, Hf, and Mg are suggested here for improved cooling at low temperatures. The time constants for the individual transition processes are evaluated and the anti-Stokes process is found to be limited by the phonon-assisted absorption time. The models (materials metrics) developed here suggest that improvements (over current record) in the cooling rate (and lowered target temperature) are possible using the identified optimal ion-host materials.

ACKNOWLEDGMENTS

The support through NSF Grant No. CTS-0553651 is greatly appreciated. We are thankful to Stephen Rand, Jasprit Singh, Xiulin Ruan, and Baoling Huang for their valuable discussions and suggestions. Philip Hebda participated in this research as an undergraduate student.

*kaviany@umich.edu

[1] P. Pringsheim, Z. Phys. **57**, 739 (1929).
[2] R. I. Epstein, M. I. Buchwald, B. C. Edwards, T. R. Gosnell, and C. E. Mungan, Nature (London) **377**, 500 (1995).
[3] X. L. Ruan, S. C. Rand, and M. Kaviany, Phys. Rev. B **75**, 214304 (2007).
[4] X. L. Ruan and M. Kaviany, J. Heat Transfer **129**, 3 (2007).
[5] B. Heeg, M. D. Stone, A. Khizhnyak, G. Rumbles, G. Mills, and P. A. DeBarber, Phys. Rev. A **70**, 021401(R) (2004).
[6] T. R. Gosnell, Opt. Lett. **24**, 1041 (1999).
[7] J. Fernandez, A. J. Garcia-Adeva, and R. Balda, Phys. Rev. Lett. **97**, 033001 (2006).
[8] D. Emin, Phys. Rev. B **76**, 024301 (2007).
[9] X. L. Ruan and M. Kaviany, J. Comput. Theor. Nanosci. **5**, 221 (2008).
[10] J. G. Solé, L. E. Bausá, and D. Jaque, *An Introduction to the Optical Spectroscopy of Inorganic Solids* (Wiley, West Sussex, 2005).
[11] G. Lei, J. E. Anderson, M. I. Buchwald, B. C. Edwards, and R. I. Epstein, Phys. Rev. B **57**, 7673 (1998).
[12] E. A. Power, *Introductory Quantum Electrodynamics* (Elsevier, New York, 1965).
[13] J. Fernandez, A. Mendioroz, A. J. Garcia, R. Balda, and J. L. Adam, Phys. Rev. B **62**, 3213 (2000).
[14] X. L. Ruan and M. Kaviany, Phys. Rev. B **73**, 155422 (2006).
[15] R. C. Powell, *Physics of Solid-State Laser Materials* (Springer-Verlag, New York, 1998).
[16] M. P. Hehlen, R. I. Epstein, and H. Inoue, Phys. Rev. B **75**, 144302 (2007).
[17] D. T. Keller, *f Electron States in Condensed Matter* (American Chemical Society, Washington, 1989), Vol. 89.
[18] S. Fraga, J. Karwowski, and K. M. S. Saxena, *Handbook of Atomic Data* (Elsevier, New York 1976).
[19] F. Herman and S. Skillman, *Atomic Structure Calculations* (Prentice-Hall, Englewood Cliffs, NJ, 1963).
[20] J. D. Axe, J. Chem. Phys. **39**, 1154 (1963).
[21] D. J. Newman, Adv. Phys. **20**, 197 (1971).
[22] B. R. Judd, Phys. Rev. **127**, 750 (1962).
[23] W. T. Carnall, H. Crosswhite, and H. M. Crosswhite, Argonne National Laboratory Report, unnumbered (1977).
[24] B. Henderson and G. F. Imbusch, *Optical Spectroscopy of Inorganic Solids* (Clarendon, Oxford, 1989).
[25] B. L. Huang and M. Kaviany, J. Appl. Phys. **100**, 123507 (2006).
[26] I. D. Feranchuk, A. A. Minkevich, and A. P. Ulyanenkov, Eur. Phys. J.: Appl. Phys. **19**, 95 (2002).
[27] N. W. Ashcroft and N. D. Mermin, *Solid State Physics* (Brooks/Cole, Belmont, 1976).
[28] A. J. Freeman and R. E. Watson, Phys. Rev. **127**, 2058 (1962).
[29] P. Blaha, K. Schwarz, G. K. H. Madsen, D. Kvasnicka, and J. Luitz, *WIEN2k, An Augmented Plane Wave+Local Orbitals Program for Calculating Crystal Properties* (Karlheinz Schwarz, Technische Uniersitat Wien, Austria, 2001).
[30] B. Handke, A. Kozlowski, K. Parlinski, J. Pzrzewoznik, T. Slezak, A. I. Chumakov, L. Niesen, Z. Kakol, and J. Korecki, Phys. Rev. B **71**, 144301 (2005).
[31] J. L. Adam, C. Ricordel, and B. Boulard, Eur. J. Solid State Inorg. Chem. **35**, 509 (1998).
[32] G. Lei, J. E. Anderson, M. I. Buchwald, B. C. Edwards, R. I. Epstein, M. T. Murtagh, and G. Sigel, Int. J. Quantum Chem. **34**, 1839 (1998).
[33] G. H. Dieke and H. M. Crosswhite, Appl. Opt. **2**, 256 (1963).
[34] L. A. Riseberg and H. W. Moos, Phys. Rev. **174**, 429 (1968).